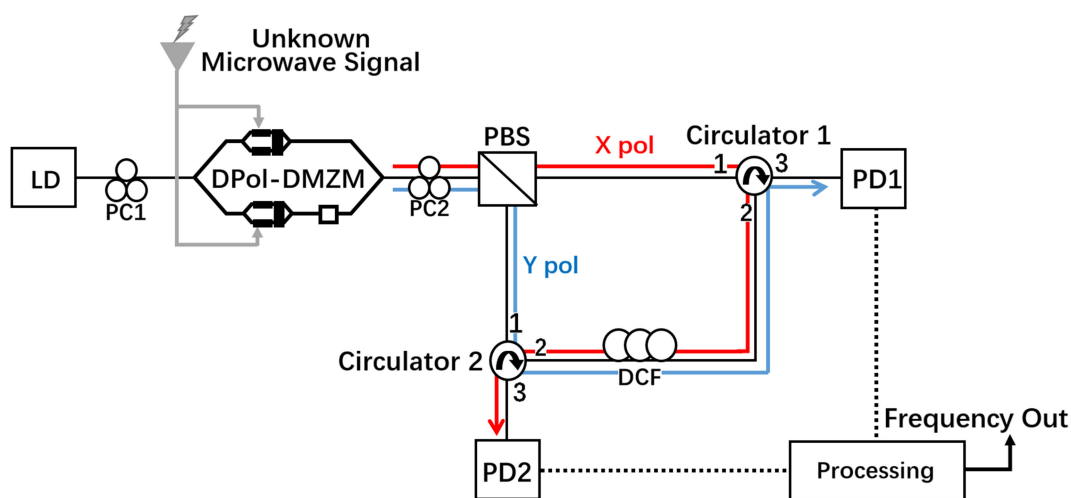# Reconfigurable Instantaneous Frequency Measurement System Based on a Polarization Multiplexing Modulator

Chengwu Yang
Wenqi Yu
Jianguo Liu, *Member, IEEE*

Reconfigurable Instantaneous Frequency Measurement System Based on a Polarization Multiplexing Modulator

Chengwu Yang [iD],[1,2] **Wenqi Yu,**[1,2]
and Jianguo Liu [iD],[1,3] *Member, IEEE*

[1]State Key Laboratory of Integrated Optoelectronics, Institute of Semiconductors, Chinese
Academy of Sciences, Beijing 100083, China
[2]College of Materials Science and Opto-Electronic Technology, University of Chinese
Academy of Sciences, Beijing 100049, China
[3]School of Electronic, Electrical and Communication Engineering, University of Chinese
Academy of Sciences, Beijing 100049, China

Abstract: We propose and demonstrate a new reconfigurable instantaneous frequency measurement (IFM) system based on a dual-polarization dual-drive Mach–Zehnder modulator (DPol-DMZM). By simply adjusting the dc biases on both arms of the DPol-DMZM, the upper and lower bounds of the IFM measurement range can be independently adjusted. Experiments have shown that the lower frequency bound is as low as 2 GHz, and the upper frequency bound is up to 23 GHz. The resolution of the three frequency measurement bandwidths of 5, 6.5, and 8 GHz is less than ± 0.2 GHz. It is noted that the proposed IFM system is power dependent. To solve this problem, a power-independent scheme with a similar system structure based on a dual-polarization dual-parallel Mach–Zehnder modulator is proposed and theoretically analyzed.

Index Terms: Microwave photonics, instantaneous frequency measurement (IFM), dual-polarization dual-drive Mach-Zehnder modulator (DPol-DMZM).

1. Introduction

Electronic warfare (EW) environments are filled with microwave signals that vary over a wide spectrum range and have a short duration. Capturing these signals and quickly identifying their parameters such as frequency, amplitude, etc., are of great importance [1]. Microwave measurements are conventionally performed using electronic devices. Despite their high resolution and high flexibility, purely electronic solutions may not be suitable for many applications due to speed and bandwidth limitations [2]. Compared with electronic techniques, the photonic-assisted techniques have the advantages of high bandwidth, low loss, light weight, and immunity to electromagnetic interference [3].

Frequency is the most basic parameter of a microwave signal. In recent years, the photonic-assisted microwave instantaneous frequency measurement (IFM) system has received extensive attention. To obtain the frequency of an unknown microwave signal, it is necessary to map the

frequency to certain optical or electrical parameters. Up to now, methods for microwave frequency measurement based on frequency-space mapping [4], [5], frequency-time mapping [6], [7], frequency-power mapping [8]–[17] have been proposed. The key to frequency-power mapping is to construct the relationship between microwave frequency and optical or electric power. In [8], a photonic approach for microwave frequency measurement using the response of cascaded infinite impulse response and finite impulse response filters was proposed. In [9]–[13], a series of methods based on amplitude comparison function (ACF) were studied. The key to these methods is to construct two complementary frequency-amplitude responses. The system in [9] uses the complementary characteristics of the transmission response and the reflection response of a fiber Bragg grating (FBG) to construct an ACF. The frequency measurement range is 1–10 GHz and the resolution slightly larger than ±0.2 GHz. Similarly, the system in [10] uses the complementary output responses of the two ports of an optical ring resonator (ORR) to construct an ACF. Using two ORRs with different Q values, resolutions of ±0.3 GHz and ±0.1 GHz are obtained in the range of 0.5–35 GHz and 1–5 GHz, respectively. The ACF can also be constructed by using the complementary output responses of the two output ports of a Mach-Zehnder interferometer (MZI) [11]. The experiment obtained a frequency measurement range of 6–18 GHz with a resolution of approximately ±0.3 GHz. To construct the ACF, system in [12] uses a complementary filter pair, which is implemented by using a polarization-maintaining fiber (PMF), in conjunction with two polarization controllers and a polarization beam splitter. The frequency measurement range of 2–24 GHz was obtained with a resolution of about ±0.2 GHz. The system in [13] uses two complementary power fading functions to construct an ACF. A frequency measurement range of 4–12 GHz was obtained with a resolution of about ±0.1 GHz. For most of the above schemes, some are inconvenient to adjust [9], [10], [12], and some have a narrow tuning range [13]. It is difficult for the schemes in [9], [10] to change the frequency measurement range, unless the core component (the FBG in [9], the OOR in [10]) is replaced. For the scheme proposed in [12], the measurement range is mainly determined by the FSR of the filter pair. A large change of the measurement range requires replacement of the PMF. The adjustability of the scheme proposed in [13] depends on the relationship between the power fading function and the wavelength, and changing the wavelength only achieves a small adjustment range.

For many applications, the IFM system needs to be reconfigured with adjustable measurement range and resolution. IFM systems with variable frequency range and resolution were widely studied. In [14], by introducing a tunable phase shift to the optical carrier of an intensity-modulated signal using stimulated-Brillouin-scattering (SBS) effect, the IFM system can be reconfigured in terms of measurement range and resolution. Similar to the scheme in [14], by adjusting the bias voltage of the modulator, the relative phase between the carrier and the sidebands can be changed, leading to an adjustable measurement range [15], [16]. A scheme based on the relationship between power fading function and wavelength of the optical carrier is proposed in [17]. The measurement range and resolution are tunable by changing the wavelength of the optical carrier. These schemes provide good guidance for changing the frequency measurement range, but there are still some issues that need to be addressed. The SBS effect was firstly introduced into the IFM system in [14], increasing the tunability of the system, but it increased the temperature-related instability of the system. The use of multiple lasers in [15], [16] also introduces additional instability. The scheme based on wavelength adjustment in [17] can only adjust the frequency measurement range over a relatively narrow range.

In this paper, a simple and novel IFM system based on a dual-polarization dual-drive Mach-Zehnder modulator (DPol-DMZM) is proposed and experimentally demonstrated. The IFM system is reconfigurable in terms of measurement range and resolution by simply adjusting the DC biases voltage of DPol-DMZM. For the measurement range obtained in the experiment, the lower frequency bound is as low as 2 GHz and the upper frequency bound is up to 23 GHz. The measurement range varies from 5 to 8 GHz with resolutions less than ±0.2 GHz. The proposed IFM system is power-dependent. To solve this problem, a power-independent scheme with similar system structure based on a dual-polarization dual-parallel Mach-Zehnder modulator (DPol-DPMZM) is proposed and theoretically analyzed.
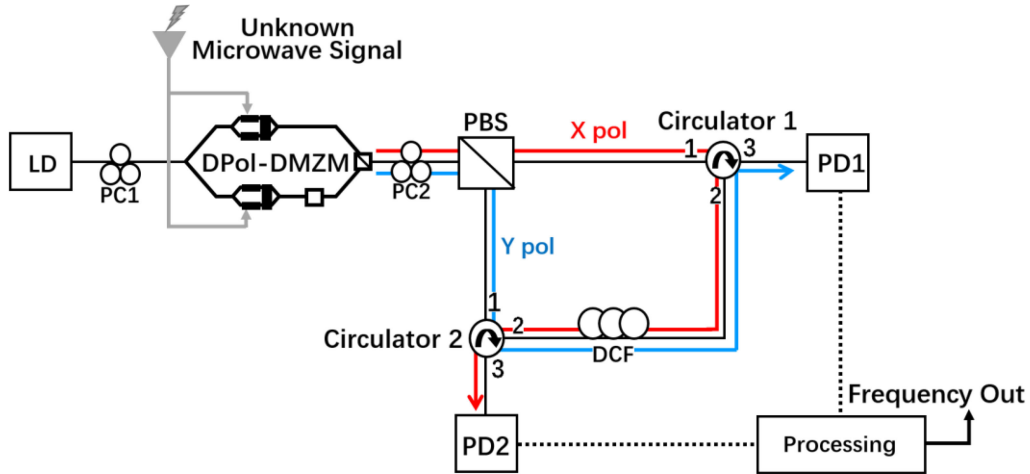
Fig. 1. Schematic configuration of the proposed IFM system.

2. Principle

The schematic configuration diagram of the proposed IFM system is shown in Fig. 1. A continuous-wave light generated by a laser diode (LD) is sent to a DPol-DMZM via a polarization controller (PC1). The unknown microwave signal is split by an RF power splitter to drive the upper and lower arms of the DPol-DMZM, respectively. Both arms are constructed with a dual-drive Mach-Zehnder modulator (DMZM).The lower arm is integrated with a 90° polarization rotator. Therefore, the modulated optical signals generated by the upper arm (DMZM1) and the lower arm (DMZM2) are polarization orthogonal. The orthogonal signals are combined by a polarization beam combiner (PBC). The output signal from the DPol-DMZM is sent to a PC (PC2) and a polarization beam splitter (PBS). The orthogonal signals from DMZM1 and DMZM2 are separated by the PBS along their respective polarization directions, and then fed to the circulators 1 and 2, respectively. A dispersion compensation fiber (DCF) is used as a dispersive element. After passing through the DCF in the opposite direction, the orthogonal signals are received by the photodetectors (PDs) to produce two independent power-fading functions, respectively. In this way, the amplitude comparison function (ACF) of the two power fading functions can be constructed to realize frequency-to-power mapping. By adjusting the DC biases of the two DMZMs, the measurement range and resolution of the system are tunable.

A key component of our scheme is the integrated DPol-DMZM, which consists of DMZM1, DMZM2, a polarization rotator and a PBC. For each DMZM, the upper arm is driven by the unknown RF signal, and the lower arm is not modulated. The relative phase shift between the two arms of each DMZM can be introduced by its DC bias. Therefore, the phase difference between the optical carrier and the sidebands can be adjusted. Fig. 2 shows the structure of DPol-DMZM, the way the signal is loaded, and spectra at different locations.

To illustrate, DMZM1 will be discussed as an example. The phase difference between the optical carrier and the sidebands introduced by the DC bias V_{DC} is frequency-independent. After passing through the dispersive medium, a frequency-dependent phase shift is introduced to the sideband with respect to the carrier. This frequency-dependent phase shift results in the power-fading effect after photodetection. Note that the power-fading function, as well as the ACF, is tunable by adjusting the frequency-independent phase shift via tuning V_{DC}. As a result, the IFM system is reconfigurable by simply adjusting V_{DC}.

As described above, the optical field from the DMZM1 is given by

$$E_{out} = \frac{E_{in}}{2} \exp j\omega_c t \cdot \exp jm \cos \omega_m t \cdot \exp j\varphi_{DC} + \frac{E_{in}}{2} \exp j\omega_c t \cdot \exp(-j\varphi_{DC}) \tag{1}$$
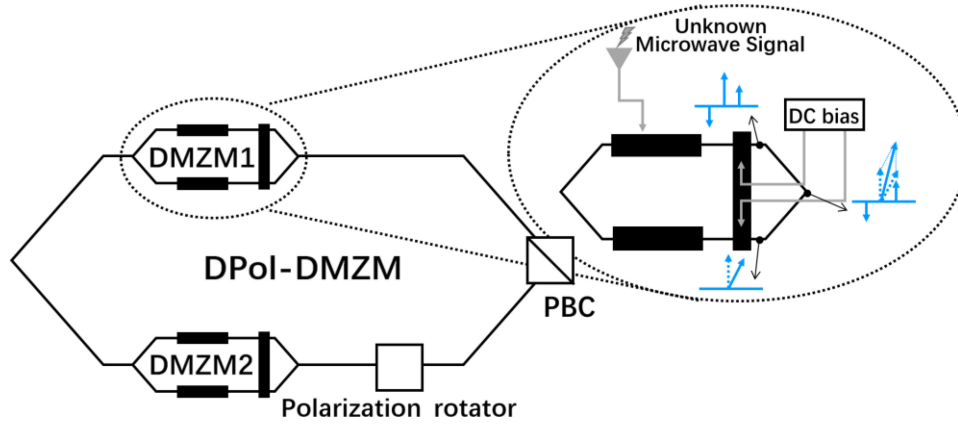
Fig. 2. The structure of DPol-DMZM, the way the signal is loaded, and spectra at different locations.

where $E_{in}\exp(j\omega_c t)$ is the input optical field. ω_m is the angular frequency of the input RF signal. $m = \pi V_m/V_\pi$ is the modulation index, which is determined by the amplitude of the RF power V_m and the half-wave voltage of the DMZM V_π. $\varphi_{DC} = \pi V_{DC}/V_\pi$ is the phase shift introduced by V_{DC1}. By applying Jacobi-Anger expansion to (1), we get

$$E_{out} = \frac{E_{in}}{2}\left\{J_0(m)\cos(\omega_c t + \varphi_{DC}) + J_1(m)\cos[(\omega_c + \omega_m)t + \varphi_{DC}]\right.$$

$$\left. + J_1(m)\cos[(\omega_c - \omega_m)t - \pi + \varphi_{DC}] + \cos(\omega_c t - \varphi_{DC})\right\} \tag{2}$$

where $J_n(\bullet)$ is the nth-order Bessel function of the first kind. After propagating the distance z in dispersive medium, the electric field is expressed as [18]

$$E_{out} = \frac{E_{in}}{2}\left\{J_0(m)\cos(\omega_c t + \varphi_{DC} + \theta_0) + J_1(m)\cos[(\omega_c + \omega_m)t + \varphi_{DC} + \theta_{+1}]\right.$$

$$\left. + J_1(m)\cos[(\omega_c - \omega_m)t - \pi + \varphi_{DC} + \theta_{+1}] + \cos(\omega_c t - \varphi_{DC} + \theta_0)\right\} \tag{3}$$

where

$$\theta_0 = z\beta_0(\omega_c) \tag{4-a}$$

$$\theta_{+1} = z\beta_0(\omega_c) + z\beta_1(\omega_c)\omega_m + \frac{1}{2}z\beta_2(\omega_c)\omega_m^2 \tag{4-b}$$

$$\theta_{-1} = z\beta_0(\omega_c) - z\beta_1(\omega_c)\omega_m + \frac{1}{2}z\beta_2(\omega_c)\omega_m^2 \tag{4-c}$$

are the additional phase of different frequency components after passing through the dispersive medium. β_n is the n-order dispersion coefficient.

After PD detection, using $I_{out} \propto E \bullet E^*$, ignoring the high-order frequency components and DC components, there is

$$I_{out} \propto \frac{1}{4}E_{in}^2 J_1(m)\left[J_0(m)\sin\left(\varphi_{DC} + \theta_0 - \frac{\theta_{+1} + \theta_{-1}}{2}\right)\right.$$

$$\left. + \sin\left(-\varphi_{DC} + \theta_0 - \frac{\theta_{+1} + \theta_{-1}}{2}\right)\right]\sin\left(\omega_m t + \frac{\theta_{+1} - \theta_{-1}}{2}\right). \tag{5}$$

Bring (4) into (5) and we have

$$I_{out} \propto \frac{1}{4}E_{in}^2 J_1(m)\left[J_0(m)\sin\left(\frac{\pi D\lambda_0^2 f_m^2}{c} - \varphi_{DC}\right) + \sin\left(\frac{\pi D\lambda_0^2 f_m^2}{c} + \varphi_{DC}\right)\right]\sin\left(\omega_m t + \frac{\theta_{+1} - \theta_{-1}}{2}\right) \tag{6}$$

where D is total fiber dispersion of DCF. λ_0 is the wavelength of optical carrier. f_m is the frequency of the input RF signal. (6) can be expressed as

$$I_{out} \propto A \cdot \sin\left[\frac{\pi D \lambda_0^2 f_m^2}{c} + f(\varphi_{DC})\right] \cdot \sin(\omega_m t + \theta_m) \tag{7}$$

where

$$A = \frac{1}{4}E_{in}^2 J_1(m)\sqrt{J_0^2(m) + 2J_0(m)\cos 2\varphi_{DC} + 1} \tag{8-a}$$

$$f(\varphi_{DC}) = \arctan\left(\frac{J_0(m) - 1}{J_0(m) + 1} \cdot \tan(\varphi_{DC})\right) \tag{8-b}$$

$$\theta_m = z\beta_1(\omega_c)\omega_m. \tag{8-c}$$

A represent the amplitude of the current produced by PD. $f(\varphi_{DC})$ represent the phase introduced by DC bias of the DMZM. θ_m represent the additional phase of the input signal after transmission. The microwave power after the PD is proportional to

$$P_{out} \propto A^2 \cdot \sin^2\left[\frac{\pi D \lambda_0^2 f_m^2}{c} + f(\varphi_{DC})\right]. \tag{9}$$

When adjusting V_{DC}, the first notch and the amplitude response of the power fading function change simultaneously. When the DC bias is fixed, A is a constant for a certain input RF power. The ACF of the two power-fading functions of the two orthogonal polarization states is given by

$$\gamma \propto \frac{A_x^2}{A_y^2} \cdot \frac{\sin^2\left[\frac{\pi D \lambda_0^2 f_m^2}{c} + f(\varphi_{DCx})\right]}{\sin^2\left[\frac{\pi D \lambda_0^2 f_m^2}{c} + f(\varphi_{DCy})\right]} \tag{10}$$

where A_x, $f(\varphi_{DCx})$, A_y, $f(\varphi_{DCy})$ represent the amplitude responses and the additional phases of the two orthogonal channels, respectively.

It can be seen from (8-a) that by selecting the appropriate RF input power $J_0(m) = 0$ can be satisfied, which makes A remain constant when V_{DC} is changed. Under this condition, (10) can be expressed as

$$\gamma \propto \frac{\sin^2\left(\frac{\pi D \lambda_0^2 f_m^2}{c} - \varphi_{DCx}\right)}{\sin^2\left(\frac{\pi D \lambda_0^2 f_m^2}{c} - \varphi_{DCy}\right)} \tag{11}$$

It can be drawn from (11) that the ACF is obtained by two power fading functions. By adjusting the bias voltage of each DMZM, the notch point of the corresponding power fading function can be tuned. The two power fading functions can be tuned independently. Therefore, the upper and lower bounds of the frequency measurement range can be adjusted independently. Fig. 3(a) shows the curves of power fading functions with the first notch located at 0-10 GHz, respectively.

With different power fading functions, the IFM system can be reconfigured with a fixed measurement bandwidth, such as 2–7 GHz, 10–15 GHz and 18–23 GHz. For a given lower measurement bound, such as 10 GHz, the measurement range can be reconfigured to such as 10–15 GHz, 10–16.5 GHz and 10–18 GHz. The simulation results of the corresponding ACFs are shown in the Fig. 3(b).

This scheme is suitable for signals of known power or constant power, such as frequency modulated (FM) signal. For unknown RF signals in other formats, there will be a large measurement error, which may limit the application of this scheme. To address this issue, the DPol-DMZM can be replaced with a dual-polarization dual-parallel Mach-Zehnder modulator (DPol-DPMZM) without changing the system structure. Fig. 4 shows the structure of a DPol-DPMZM [19]. The DPol-DPMZM consists of a PBS, two DPMZMs (DPMZM1 and DPMZM2) and a PBC. Each DPMZM consists of two sub-MZMs (MZM1 and MZM2) placed parallel in a parent-MZM (MZM3). For DPMZM1, MZM1
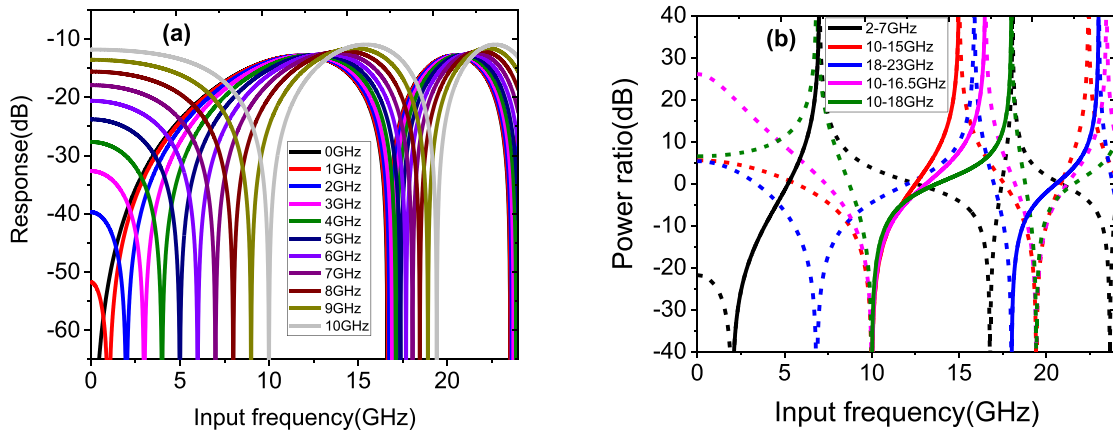
Fig. 3. (a) Simulated power fading functions. (b) The simulated ACFs of different measurement ranges. The solid lines represent the sections for measurement, and the dashed lines represent the unused sections.
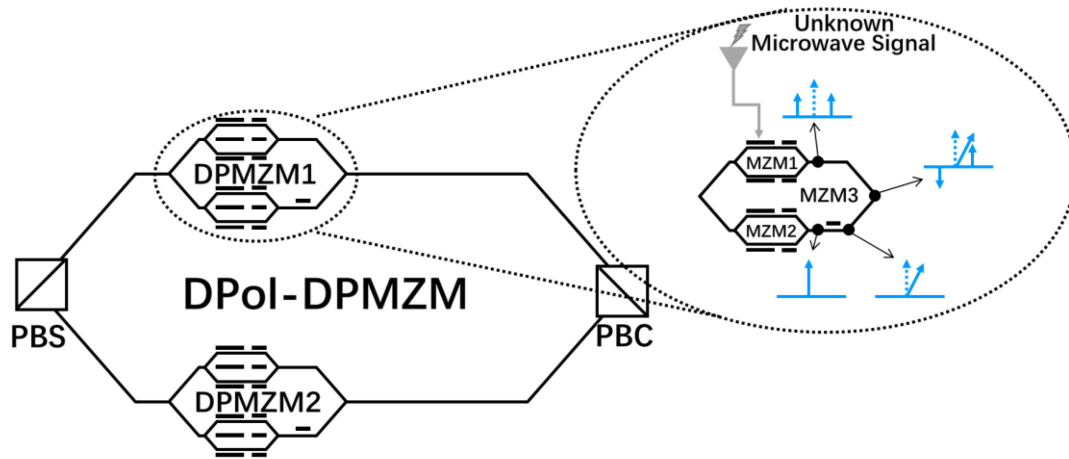

Fig. 4. The structure of DPol-DPMZM, the way the signal is loaded, and spectra at different locations.

is biased at minimum transmission to implement carrier-suppressed double-sideband (CS-DSB) modulation. MZM2 has no driven signal and is biased at the maximum transmission point to allow the optical carrier to pass through. The relative phase of CS-DSB signal and the optical carrier is controlled by the DC bias of MZM3. The input signal is loaded to DPMZM1 and DPMZM2 in the same way. The detailed derivation of the formula is given in [15]. Based on the previous derivation, the response of one of the polarization channels is

$$P_{out} \propto B \cdot \cos^2\left(\frac{\pi D \lambda_0^2 f_m^2}{c} - \varphi_{DC3}\right) \tag{12-a}$$

$$B = 4J_1^2(m)\cos^2\varphi_{DC2} \tag{12-b}$$

where φ_{DC2} and φ_{DC3} are the DC bias of MZM2 and MZM3, respectively. B remains unchanged when φ_{DC3} changes. By comparing (9) and (12), we can find that the ACF obtained based on the DPol-DPMZM modulator is independent of the input RF power. Due to the lack of such a DPol-DPMZM, our laboratory currently does not have the conditions for this experiment. Only the theory is analyzed here.
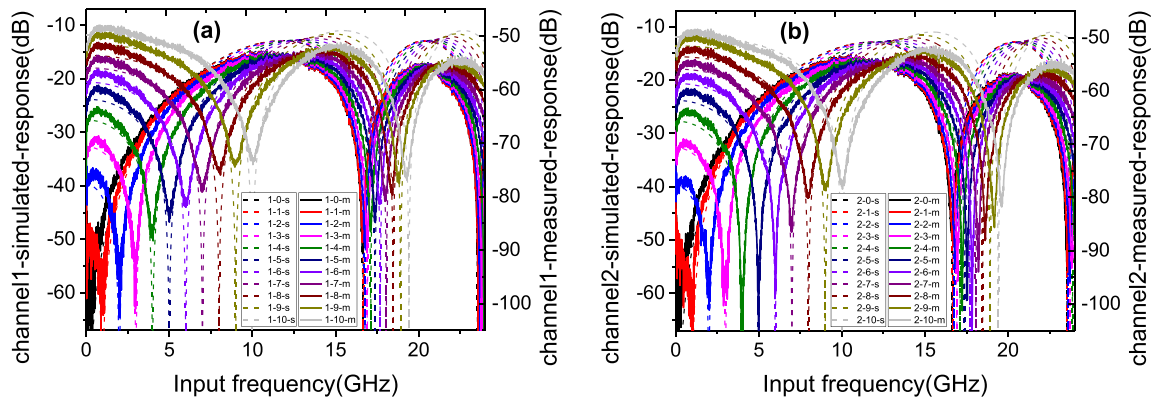
Fig. 5. The measured (solid lines) and simulated (dash lines) power-fading functions for (a) channel 1 (X-pol) and (b) channel 2 (Y-pol).
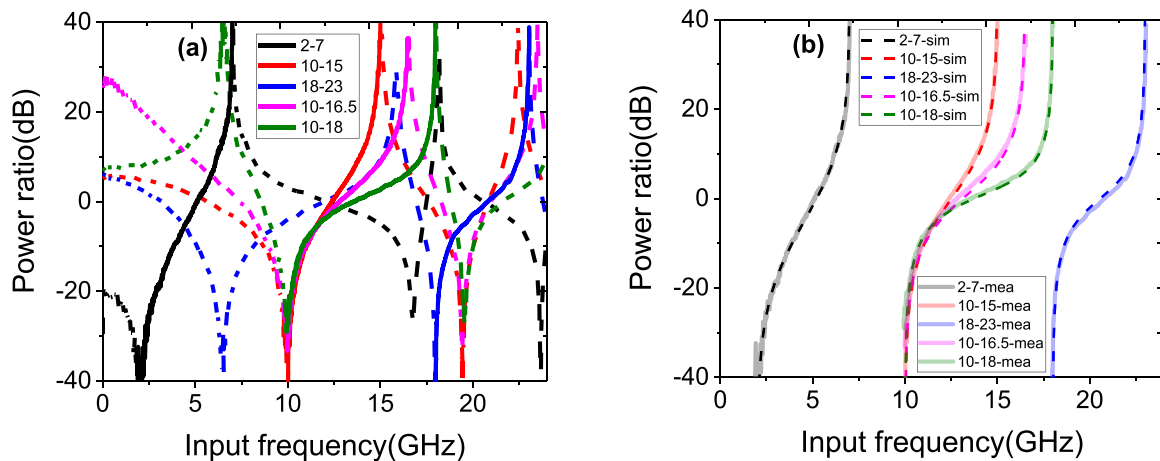

Fig. 6. (a) The measured ACFs. The solid lines represent the sections for measurement, and the dashed lines represent the unused sections. (b) The comparison between the measured ACFs (solid lines) and the simulated ACFs (dash lines).

3. Experiments

A continuous wave (CW) laser at a wavelength of 1549.974 nm was produced by a commercial laser device (Yenista Optics, TUNICS T100S-HP). The output power was 10 dBm. The most bandwidth-limiting component in our experiment is the DPol-DMZM (Fujitsu FTM7980EDA) with a 3 dB bandwidth of 20 GHz. The 5 km DCF has a total dispersion of −450.5 ps/nm. The bandwidths of the PDs (Optlab, LR-40) are 40 GHz.

The power-fading functions were captured by a vector network analyzer (VNA). The output power of the continuous-wave electrical signal from the VNA was 5 dBm. Fig. 5(a) and (b) show the measured (solid lines) and the simulated (dash lines) power-fading functions for channel 1 (X-pol) and channel 2 (Y-pol), respectively. Experimental results match well with the theoretical prediction. Compared to the simulation results, the measured curve will tilt slightly downward due to the large link loss at high frequencies.

Five frequency measurement ranges were chosen to verify theoretical results, 2–7 GHz, 10–15 GHz, 18–23 GHz, 10–16.5 GHz and 10–18 GHz, respectively. The measured results of the corresponding ACFs are shown in the Fig. 6(a). The comparison between the measurement results
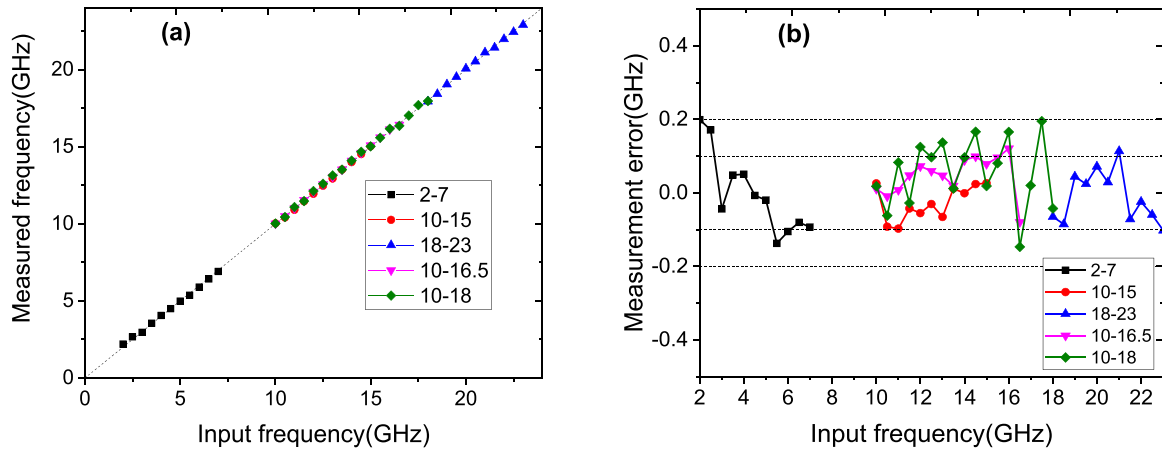
Fig. 7. (a) Measured frequency versus input frequency and (b) the measurement error as a function of input frequency for different measurement ranges.

TABLE 1
Measurement Range and Resolution

Measurement range(GHz)	2-7	10-15	18-23	10-16.5	10-18
Resolution(GHz)	$\pm$0.2	$\pm$0.1	$\pm$0.12	$\pm$0.12	$\pm$0.2

(solid lines) and the simulation results (dash lines) are shown in Fig.6(b). The experimental results are in good agreement with the theoretical predictions.

Fig. 7 shows the measurement error as a function of the input frequency for different measurement ranges. For a fixed measurement bandwidth of 5 GHz, 2–7 GHz, 10–15 GHz and 18–23 GHz, the resolutions are $\pm$0.2 GHz, $\pm$0.1 GHz and $\pm$0.12 GHz, respectively. The higher the slope of the power-frequency mapping curve, the higher the accuracy of the frequency measurement, which means better resolution near the notch. It should be noted that the power fluctuation at the notch brings a large error. The measurement error in the middle part of the 2–7 GHz measurement range is within $\pm$0.1 GHz. For the frequency measurement ranges with a fixed lower measurement bound of 10 GHz, 10–15 GHz, 10–16.5 GHz and 10–18 GHz, the resolutions are $\pm$0.1 GHz, $\pm$0.12 GHz and $\pm$0.2 GHz, respectively. Generally, a small measurement range corresponds to a low measurement error. The results in Fig. 7(b) and Table 1 verify this conclusion.

4. Discussion

System instability will result in measurement errors in the IFM system. The measured frequency of the unknown signal corresponds to the value of the ACF. Therefore, the measurement errors depend on the instability of the ACF. Considering the use of a logarithmic unit system, the ACF can be written as

$$y = 10 \lg \left[\frac{\sin^2 \left(\frac{\pi D \lambda_0^2 f_m^2}{c} - \varphi_{DCx} \right)}{\sin^2 \left(\frac{\pi D \lambda_0^2 f_m^2}{c} - \varphi_{DCy} \right)} \right]. \tag{13}$$

According to (13), the ACF is directly affected by the dispersion value of the DCF, the wavelength of the laser, and the additional phase determined by the DC bias. These parameters are mainly influenced by the temperature fluctuation. The DCF is equivalent to a longer dispersion-shifted single-mode fiber (DS-SMF). The DS-SMF has a dispersion slope of 0.08 ps/km·nm^2, which hardly
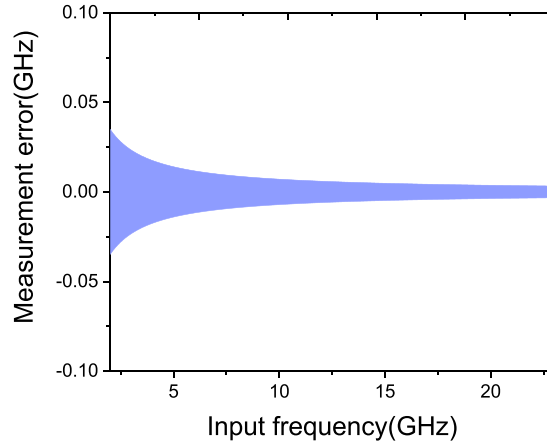
Fig. 8. Theoretical temperature induced measurement error for a temperature fluctuation of ± 0.12 °C.

changes with temperature. The zero-dispersion wavelength of the fiber is affected by temperature fluctuation, and the coefficient is about 0.03 nm/°C [20]. The laser has its own temperature control system. Therefore, the stability of the laser wavelength is independent of temperature. The instability of the laser wavelength in 24 hours is ± 5 pm [21]. For LiNbO$_3$ modulators, the bias drift is about 5V when the temperature varies from -5 to 80 °C [22]. It is assumed that the bias voltage drifts uniformly with temperature.

The uncertainty of the ACF $\triangle y$ can be expressed as

$$\Delta y = \left| \frac{\partial y}{\partial D} \right| \cdot \Delta D + \left| \frac{\partial y}{\partial \lambda_0} \right| \cdot \Delta \lambda_0 + \left| \frac{\partial y}{\partial \varphi} \right| \cdot \Delta \varphi_{DC} \tag{14}$$

where ΔD, $\Delta \lambda_0$, $\Delta \varphi_{DC}$ represent the uncertainty of D, λ_0, and $\varphi_{DC(x/y)}$, respectively. $|\partial y/\partial D|$, $|\partial y/\partial \lambda_0|$, $|\partial y/\partial \varphi_{DC}|$ represent the error transfer coefficient of D, λ_0, and $\varphi_{DC(x/y)}$, respectively. The two DMZMs of X-pol and Y-pol are integrated in one device. Their bias drifts are considered equal.

The frequency measurement error Δf_m can be written as

$$\Delta f_m = \Delta y / \left(\frac{\partial y}{\partial f} \right) \tag{15}$$

where $\partial y / \partial f$ is the slope of ACF.

For the range of 2–23 GHz, when the temperature fluctuation is ± 0.4 °C and ± 0.7 °C, the theoretical errors are ± 0.1 GHz and ± 0.2 GHz, respectively. The temperature stability of ± 0.12 °C can be easily achieved using a commercially available temperature controller [12]. When the temperature changes within ± 0.12 °C, the values of ΔD, $\Delta \lambda_0$, and $\Delta \varphi_{DC}$ are ± 0.0058 ps/nm, ± 5 pm and ± 0.0016 rad, respectively. Fig. 8 shows the theoretical temperature induced measurement error for a temperature fluctuation of ± 0.12 °C. It can be drawn that the temperature fluctuation has a greater impact on low frequencies.

Moreover, instability may cause jitter in the display value of the instrument. In experiment, the jitter of the display value is about 0.2dB. According to (15), the measurement error can be calculated with a fixed display jitter Δy. Fig. 9 shows the measurement error versus input frequency when the display jitter Δy changes from ± 0.1 to ± 0.3 dB. It can be drawn that there is a trade-off between the measurement range and resolution. In areas where the ACF changes relatively large, the measurement error is small.

In addition, the polarization states before the DPol-DMZM and the PBS will drift due to environment factors. The polarization state of the optical input is forced to align with the slow-axis of the input fiber by the DPol-DMZM. The polarization drift before the modulator will change the effective input optical power. According to Eq. (12), the ACF is independent of the input optical power. So
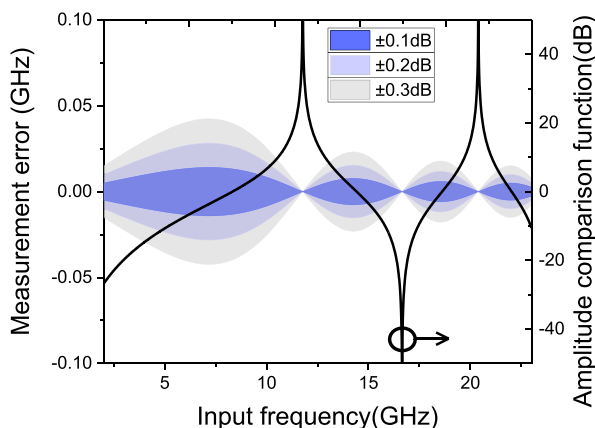
Fig. 9. Theoretical measurement error range when the instrument's uncertainty is ± 0.1 dB to ± 0.3 dB.

the polarization drift before the DPol-DMZM does not affect the measurement results. However, according to our analysis, the notch points of the two power fading functions will move due to polarization drift before the PBS. Consequently, the measured value of the frequency will deviate from the actual value. In fact, we have observed the polarization states of the polarization-orthogonal optical signals before and after measurement. Because the laboratory environment was relatively stable, there was no significant change in polarization after nearly 30 minutes. Under harsh conditions, the polarization states are very likely to drift due to vibration or temperature change. The polarization drift before PBS will result in large measurement error.

5. Conclusion

We propose an IFM system based on a polarization multiplexing modulator. A DPol-DMZM is used, which consists of two polarization multiplexed DMZMs. Two polarization-orthogonal signals are produced by the DMZMs, respectively. For each signal, the relative phase shift between the optical carrier and the sidebands can be independently adjusted by varying the DC bias of each DMZM. The relative phase shift is frequency-independent. After passing through the dispersive medium, a frequency-dependent phase shift is introduced to the sideband relative to the carrier. This frequency-dependent phase shift results in a power-fading effect after photodetection. By adjusting the DC bias of the corresponding DMZM, the position of the first notch of the power fading curve can be adjusted. Two independent power fading curves can be obtained by the orthogonal signals. Finally, the ACF of the two curves can be constructed. The lower and upper frequency bounds of the measurement range can be adjusted independently.

A proof-of-concept demonstration of the proposed technique has been presented. For a fixed measurement bandwidth of 5 GHz, 2–7 GHz, 10–15 GHz and 18–23 GHz, the resolutions were ± 0.2 GHz, ± 0.1 GHz and ± 0.12 GHz, respectively. For a given lower measurement bound, 10–15 GHz, 10–16.5 GHz and 10–18 GHz, the resolution were ± 0.1 GHz, ± 0.12 GHz and ± 0.2 GHz, respectively. It can be concluded that a small bandwidth corresponds to a high resolution. It is assumed that the frequency of the unknown signal varies over a wide range and the measurement requires high resolution. Usually a single IFM system cannot meet both requirements at the same time. For this situation, we propose to use multiple IFM systems in parallel. The measurement range of the proposed IFM system can be flexibly reconfigured. For example, the measurement ranges of the IFM systems are set to 2–7 GHz, 7–12 GHz, 12–17 GHz, 17–22 GHz. A measurement range of 20 GHz can be obtained with high resolution. One issue is that each IFM system will provide a power ratio. This makes it difficult to tell the true input frequency. Regarding this issue, two solutions are currently conceivable. The first method is to add an electrical filter before each IFM system. The

passband of each electrical filter is the same as the immediately following IFM system. DC-blocking PDs are used. Only one power ratio will be obtained. The second method is to combine a wide-range, low-resolution IFM system with the parallel IFM systems. The former roughly locates the frequency of the microwave to be measured, and the latter gives the final high-precision outputs. Among the multiple outputs of the parallel IFM systems, the one closest to the rough measurement result is selected as final result.

The proposed IFM system is power-dependent. To address this issue, the DPol-DMZM is replaced by a DPol-DPMZM. By adjusting the DC biases of the DPol-DPMZM, the measurement range of the system can be reconfigured. The IFM system is independent of RF input power. Theoretical analysis is given.

References

[1] S. Pan, J. Fu, and J. Yao, "Photonic approach to the simultaneous measurement of the frequency, amplitude, pulse width, and time of arrival of a microwave signal," *Opt. Lett.*, vol. 37, no. 1, pp. 7–9, 2012.

[2] S. Pan and J. Yao, "Photonics-based broadband microwave measurement," *J. Lightw. Technol.*, vol. 35, no. 16, pp. 3498–3513, Aug. 2017.

[3] J. Yao, "Microwave photonics," *J. Lightw. Technol.*, vol. 27, no. 3, pp. 314–335, Feb. 2009.

[4] S. T. Winnall *et al.*, "A microwave channelizer and spectroscope based on an integrated optical Bragg-grating Fabry-Perot and integrated hybrid Fresnel lens system," *IEEE Trans. Microw. Theory Techn.*, vol. 54, no. 2, pp. 868–872, Feb. 2006.

[5] W. Wang *et al.*, "Characterization of a coherent optical RF channelizer based on a diffraction grating," *IEEE Trans. Microw. Theory Techn.*, vol. 49, no. 10, pp. 1996–2001, Oct. 2001.

[6] L. V. T. Nguyen, "Microwave photonic technique for frequency measurement of simultaneous signals," *IEEE Photon. Technol. Lett.*, vol. 21, no. 10, pp. 642–644, May 2009.

[7] T. A. Nguyen, E. H. W. Chan, and R. A. Minasian, "Instantaneous high-resolution multiple-frequency measurement system based on frequency-to-time mapping technique," *Opt. Lett.*, vol. 39, no. 8, pp. 2419–2422, 2014.

[8] J. Zhou *et al.*, "Instantaneous microwave frequency measurement using a photonic microwave filter with an infinite impulse response," *IEEE Photon. Technol. Lett.*, vol. 22, no. 10, pp. 682–684, May 2010.

[9] Z. Li *et al.*, "Instantaneous microwave frequency measurement using a special fiber Bragg grating," *IEEE Microw. Wireless Compon. Lett.*, vol. 21, no. 1, pp. 52–54, Jan. 2011.

[10] J. Jiang *et al.*, "Photonic-assisted microwave frequency measurement system based on a silicon ORR," *Opt. Commun.*, vol. 382, pp. 366–370, 2017.

[11] J. Dai *et al.*, "A simple photonic-assisted microwave frequency measurement system based on MZI with tunable measurement range and high resolution," *IEEE Photon. Technol. Lett.*, vol. 22, no. 15, pp. 1162–1164, Aug. 2010.

[12] X. Zou, H. Chi, and J. Yao, "Microwave frequency measurement based on optical power monitoring using a complementary optical filter pair," *IEEE Trans. Microw. Theory Techn.*, vol. 57, no. 2, pp. 505–511, Feb. 2009.

[13] L. V. T. Nguyen and B. H. David, "A photonic technique for microwave frequency measurement," *IEEE Photon. Technol. Lett.*, vol. 18, no. 10, pp. 1188–1190, May 2006.

[14] W. Li, N. H. Zhu, and L. X. Wang, "Brillouin-assisted microwave frequency measurement with adjustable measurement range and resolution," *Opt. Lett.*, vol. 37, no. 2, pp. 166–168, 2012.

[15] W. Li, N. H. Zhu, and L. X. Wang, "Reconfigurable instantaneous frequency measurement system based on dual-parallel Mach–Zehnder modulator," *IEEE Photon. J.*, vol. 4, no. 2, pp. 427–436, Apr. 2012.

[16] H. Zhang and S. Pan, "High resolution microwave frequency measurement using a dual-parallel Mach–Zehnder modulator," *IEEE Microw. Wireless Compon. Lett.*, vol. 23, no. 11, pp. 623–625, Nov. 2013.

[17] J. Li *et al.*, "Photonic-assisted microwave frequency measurement with higher resolution and tunable range," *Opt. Lett.*, vol. 34, no. 6, pp. 743–745, 2009.

[18] H. Zhang *et al.*, "Polarization-modulated analog photonic link with compensation of the dispersion-induced power fading," *Opt. Lett.*, vol. 37, no. 5, pp. 866–868, 2012.

[19] W. T. Wang *et al.*, "Phase-coherent orthogonally polarized optical single sideband modulation with arbitrarily tunable optical carrier-to-sideband ratio," *Opt. Exp.*, vol. 24, no. 1, pp. 388–399, 2016.

[20] J. P. Kilmer, W. T. Anderson, and A. J. Johnson, "Chromatic dispersion temperature dependence of matched-clad, depressed-clad, and dispersion-shifted single-mode fibers," *Proc. SPIE*, vol. 841, pp. 274–278, 1987.

[21] 2018. [Online]. Available: https://www.exfo.com/umbraco/surface/file/download/?ni=17917&cn=en-US&pi=17918

[22] T. Shiraishi *et al.*, "Suppression of thermal drift in an ultra-high-speed LiNbO$_3$ optical modulator," in *Proc. IEEE Lasers Electro-Opt. Soc. Annu. Meeting*, 2007, pp. 169–170.